Magnetic resonance safety and compatibility of tantalum markers used in proton beam therapy for intraocular tumors: a 7.0 Tesla study

Oberacker, E. and Paul, K. and Huelnhagen, T. and Oezerdem, C. and Winter, L. and Pohlmann, A. and Boehmert, L. and Stachs, O. and Heufelder, J. and Weber, A. and Rehak, M. and Seibel, I. and Niendorf, T.

Oberacker, E., Paul, K., Huelnhagen, T., Oezerdem, C., Winter, L., Pohlmann, A., Boehmert, L., Stachs, O., Heufelder, J., Weber, A., Rehak, M., Seibel, I. and Niendorf, T. (2017), Magnetic resonance safety and compatibility of tantalum markers used in proton beam therapy for intraocular tumors: A 7.0 Tesla study. Magn. Reson. Med., 78: 1533–1546. doi:10.1002/mrm.26534

which has been published in final form in:

Magnetic Resonance in Medicine
2017 OCT; 78(4): 1533–1546
2016 NOV 10 (first published online)
doi: 10.1002/mrm.26534

Publisher: Wiley-Blackwell

Magnetic resonance safety and compatibility of tantalum markers used in proton beam therapy for intraocular tumors: A 7.0 Tesla study

Eva Oberacker[1], Katharina Paul[1], Till Huelnhagen[1], Celal Oezerdem[1], Lukas Winter[1], Andreas Pohlmann[1], Laura Boehmert[1], Oliver Stachs[2], Jens Heufelder[3], Andreas Weber[3], Matus Rehak[4], Ira Seibel[4], Thoralf Niendorf[1,5]

[1]Berlin Ultrahigh Field Facility (B.U.F.F.), Max Delbrück Center for Molecular Medicine in the Helmholtz Association, Berlin, Germany, [2]Department of Ophthalmology, University of Rostock, Rostock, Germany, [3]Charité – Universitätsmedizin Berlin, BerlinProtonen am HZB, Berlin Germany, [4]Charité – Universitätsmedizin Berlin, Klinik für Augenheilkunde Campus Benjamin Franklin, Berlin, Germany, [5]Experimental and Clinical Research Center (ECRC), a joint cooperation between the Charité Medical Faculty and the Max Delbrück Center for Molecular Medicine in the Helmholtz Association, Berlin, Germany

Correspondence to:
Prof. Dr. Thoralf Niendorf
Berlin Ultrahigh Field Facility (B.U.F.F.)
Max Delbrück Center for Molecular Medicine
Robert-Roessle-Strasse 10
13125 Berlin
Germany
phone: +49 30 9406 4505
fax: +49 30 9406 49178
e-mail: thoralf.niendorf@mdc-berlin.de

Running title: MR safety of ocular tantalum markers measured at 7.0 Tesla

Key words: ophthalmic imaging, magnetic resonance imaging, ultrahigh field MR, uveal melanoma, proton therapy

Word count: 5708

Abstract

Purpose: Proton radiation therapy (PRT) is a standard treatment of uveal melanoma. PRT patients undergo implantation of ocular tantalum markers (OTMs) for treatment planning. Ultrahigh field MRI is a promising technique for 3D tumor visualization and PRT planning. This work examines MR safety and compatibility of OTMs at 7.0 Tesla.

Methods: MR safety assessment included deflection angle measurements (DAM), electromagnetic field (EMF) simulations for SAR estimation and temperature simulations for examining RF heating using a bow tie antenna for transmission. MR compatibility was assessed via susceptibility artifacts in agarose, ex-vivo pig eyes and in an ex-vivo tumor eye employing gradient echo and fast spin-echo imaging.

Results: DAM (α<1°) demonstrated no risk due to magnetically-induced OTM deflection. EMF simulations showed that an OTM can be approximated by a disk, demonstrated the need for averaging masses of m_{ave}=0.01g to accommodate the OTM, and provided $SAR_{0.01g,maximum}$=2.64 W/kg (P_{in}=1W) in OTM presence.A transfer function was derived, enabling $SAR_{0.01g}$-estimation for individual patient scenarios without the OTM being integrated. Thermal simulations revealed minor OTM related temperature increase (δT<15 mK). Susceptibility artifact size (<8 mm) and location suggest no restrictions for MRI of the nervus opticus. .

Conclusion: OTMs are not a *per-se* contraindication for MRI.

Introduction

Proton radiation therapy (PRT) is one of the standard therapeutic approaches applied to patients suffering from uveal melanoma, the most prevalent primary intraocular malignancy world-wide with an incidence of ≈1/100,000 new cases per year (1-6). PRT of ocular tumors has been performed in >28,000 patients (7-9). Most of the ocular tumor patients scheduled for PRT undergo an implantation of ocular tantalum markers (OTM) which are sutured to the sclera (10, 11) and used in tumor localization, treatment planning and patient positioning prior to irradiation (11-14).

Progress in magnetic resonance imaging (MRI) has permitted advances in the diagnosis of malignant melanomas of the uveal tract and planning of PRT. The spatial resolution and tissue contrast benefits of MRI versus A- and B-scan ultrasound measurements and low tissue contrast computed tomography permit a clearer delineation of the tumor margins (15). However, the delineation of an extrascleral extension and the assessment of tumor invasion into the optic nerve or the vortex veins continues to pose a challenge for radiation planning and radiotherapy directed at ocular tumors (3, 16). This challenge is due to spatial resolution constraints of MRI at 1.5 T and 3.0 T. Given the gain in spatial resolution in ultrahigh field (UHF) MRI ($B_0 \geq 7.0$ T) it is conceptually appealing for *in vivo* imaging, 3D visualization and PRT planning in cases of uveal melanoma (17-24).

A broad spectrum of conducting implants have been declared MR safe (25), but to the best of our knowledge no data has been published on the MR safety and MR compatibility of OTMs. A detailed analysis of MR safety and MR compatibility of OTMs will play a key role in whether the potentially powerful combination of UHF-MR guided PRT advances or is dismissed.

Realizing the safety requirements and the clinical opportunities of ophthalmic MRI, this work examines the MR safety and MR compatibility of OTMs. Recognizing the underserved clinical needs we hypothesize that MRI in the presence of OTMs would cause radiofrequency (RF) induced temperature increase and displacement that does not exceed regulatory limits and RF exposure guidelines (26, 27) at 7.0 T. To test this hypothesis, we examined radiofrequency heating, magnetically induced displacement and artifact formation caused by magnetic susceptibility.

Methods

Ocular tantalum marker

OTMs are button-like implants sutured to the sclera of the diseased eye close to the tumor (Fig.1a,b). Placement on the dorsal half of the eye is often chosen to increase patient comfort while blinking and to avoid radiation loss in the umbra of the metallic implant. OTM implantation commonly involves four markers, three of which are placed close to the borders of the tumor mass (Fig.1b). The position of the fourth marker is usually diametrically opposed so that small eye movements can be monitored (Fig.1b). Implant parameters are: Altomed Limited (Boldon, Tyne and Wear, England), diameter D=2.5 mm, thickness=0.17 mm, two holes with D=0.85 mm, weight=$m_{implant}$=17.1 mg (Fig.1a). The OTMs investigated in this study were obtained from the only manufacturer providing CE certification for the use of the markers in proton beam therapy of ocular tumors.

Magnetically induced displacement

The displacement force induced by the magnetic field gradient was evaluated using the deflection method (28). An OTM was hung on an in-house built holder, equipped with a hook to hold the implant at the center of an angular gauge (radius of curvature ~25 cm). A polyester USP 9-0 suture (Ethicon INC, Johnson&Johnson Medical GmbH, Norderstedt, Germany, D=30 µm, m_{suture}=30 ng, m_{thread}<1% of m_{OTM}) was used (28). The setup was placed at the front end of a 7.0 T human MR system (Magnetom, Siemens Healthcare, Erlangen, Germany) where the B_0 gradient is strongest (dB/dz≈5 T/m).

Radiofrequency induced heating

Radiofrequency-induced heating was evaluated by assessing specific absorption rate (SAR) and temperature in the tissue simulating material (TSM) in the presence of an OTM using IEC limits for safe operation as a reference (26, 27).

Electromagnetic field (EMF) simulations were conducted with the finite difference time domain method (Sim4Life V2.0, ZMT, Zurich, Switzerland). The virtual implant was placed in a rectangular phantom model (Fig.1c) filled with TSM resembling the conductivity of the sclera (σ=0.94 S/m, ε=79, ρ=1.041 g/cm³) (29). A meshbox (isotropic resolution=0.05 mm, size=(10x10x10) mm³) was defined around the OTM. This high resolution mesh box was encased by a region (isotropic resolution=0.1 mm, size=(15x15x32.5) mm³) to save CPU time. This setup was placed underneath the center of a virtual bowtie electric dipole RF antenna (l=15 cm, (30)) used for RF transmission ($P_{in,\ peak}$=1 W) (Fig.1c). This approach yields well defined E-field vectors in relation to the positioning of the implant (31).

If an electrically conductive passive implant such as an OTM is subjected to an incident electric field, surface currents and charges must be induced to superimpose a scattered E-field on the incident E-field to meet the boundary condition $\vec{E}_{\tan}\big|_{\text{total}} = \vec{E}_{\tan}\big|_{\text{inc}} + \vec{E}_{\tan}\big|_{\text{sca}} = 0$ (32). The superposition of $\vec{E}_{\text{inc}}$and $\vec{E}_{\text{sca}}$ might

lead to a local increase in absolute E-fields $|\vec{E}|$, which increase $SAR \propto |\vec{E}|^2$ (32). E-field coupling was investigated for the button like geometry of the implant, which was modeled as a perfect electric conductor (PEC). We investigated the influence of the orientation ϑ of the holes with respect to the electric field lines on the surface current induced on the implant as well as on the RF power deposition for ϑ_1=0°, ϑ_2=45° and ϑ_3=90°. As a mean of generalization for differing implant orientation, we studied the E-field coupling to a disk (PEC) with the same outer dimensions as the implant. To resemble the positioning of the OTMs on the eye globe (Fig.1b), the distance d between the antenna and the OTM was varied (d=15-30 mm, increment=2.5 mm). The spherical shape of the globe was taken into account by introducing rotations ranging from 0° to 90° (increment=15°) with the rotation axis parallel ($\gamma_\parallel$) and perpendicular ($\gamma_\perp$) to the electric field lines at a representative distance of 25 mm.

For SAR assessments, it is common to use the local SAR (SAR_{10g}) averaged over 10 g of tissue (26). This tissue volume largely exceeds the size of an OTM and bears the risk of heavy underestimation of local peak SAR (31, 33, 34). To address this issue, a smaller averaging volume is required. Consequently, SAR_{10g} was not included in the SAR evaluation. Point SAR quantifies the power deposited in a volume as small as the simulated resolution. While this provides high spatial accuracy, it is highly susceptible to changes in simulated mesh size. Not only does the peak SAR changes significantly with rather small changes in mesh size, this also constitutes a challenge for the comparability of the acquired data. For these reasons, we employed discrete SAR averaging masses ranging from m_{ave}=1 g to m_{ave}=0.01 g.

The temperature distribution near the OTM was evaluated in thermal simulations employing Pennes' Bioheat equation, an FDTD solver (Sim4Life V2.0, ZMT, Zurich, Switzerland) and the virtual phantom in conjunction with the virtual RF antenna setup used for the EMF simulations. Thermal simulations were performed for one disk position at a distance of d=25 mm from the bow tie antenna, and parallel ($\gamma_\parallel$=$\gamma_\perp$=0°) to its main axis. This position was chosen based on strong expected interaction ($\gamma_\parallel$=$\gamma_\perp$=0°) while being less prone to overlapping with the surface heating of a bow tie antenna (31). The thermal conductivity and heat capacity of the tissue simulating material (TSM) were k=0.53 W/(m·K) and c=3546 J/(kg·K) to mimic the thermal properties of the sclera (29). An input power of P_{in}=1 W was applied at the bow tie antenna for a duration of t_1=6 min and t_2=15 min.

Further simulations were conducted by scaling P_{in} according to the normal operating mode governed by the IEC guidelines at the position of SAR_{max} for $SAR_{0.01g}$=10 W/kg and SAR_{1g}=10 W/kg. Only locations with sufficient distance to the surface were included in the evaluation, ensuring SAR averaging in the homogeneous TSM only. In the same way, the 1st level controlled mode

(SAR_{ave}=20 W/kg) was simulated, scaled to $SAR_{0.01g}$ as well as SAR_{1g}. Based on these data, an extra simulation was scaled to reach a maximum temperature increase of ΔT_{max}=1 K.

Imaging artifacts in phantoms

To investigate susceptibility-induced artifacts at implant/tissue interfaces, a head shaped phantom was constructed. Two spherical holders were incorporated at the position of the eyes to accommodate an agarose sample (2% Agarose (SeaPaque GTG Agarose, Lonza, Rockland, ME, USA); Fig.1d) containing one OTM. Phantom experiments were performed on a 7.0 T whole-body MR system (Magnetom, Siemens Healthcare, Erlangen, Germany). A dedicated six-element transceiver array was employed for signal transmission/reception (TX/RX) (35). Simulated maximum SAR_{1g} in the human voxel model was found to be SAR_{1g}(Duke)=4.1 W/kg and SAR_{1g}(Ella)=3.7 W/kg for P_{in}=1W, not taking into account the losses in the interfaces upstream of the TX/RX array. Artifact size and shape were investigated using two imaging protocols:

- T_1-weighted gradient echo (GRE):FOV=70 mm, matrix size=256x256, in-plane spatial resolution=0.3 mm, slice thickness=1.0 mm, 32 slices, BW=300 Hz/Px, nominal flip angle=4°, TR=30 ms, TE=3.9 ms.
- T_2-weighted RARE: FOV=70 mm, matrix size=256x256, in-plane spatial resolution=0.3 mm, slice thickness=1.0 mm, 32 slices, BW=300 Hz/Px, nominal refocusing flip angle=120°, TR=3000 ms, TE=55 ms, echo train length=12.

For each protocol two acquisitions were performed: one with the OTM positioned parallel to $B_{0,}$ and one perpendicular to B_0 as suggested by the ASTM standard on the evaluation of MR image artifacts of passive implants (36).

Imaging artifacts in ex vivo porcine eyes

To establish conditions closer to the clinical scenario, susceptibility artifacts in ex vivo pigs' eyes were evaluated. Three OTMs were sutured to the sclera in positions resembling those of markers in PRT (12-14). The eye was then placed in the lower half shell of the spherical holder incorporated into the head-shaped phantom. After placing the upper half shell, the eye was bathed with a phosphate buffer saline (PBS) solution (Biochrom AG, Berlin, Germany) to eliminate susceptibility artifacts caused by air bubbles and hydration. Imaging was first performed at 7.0 T using the MR hardware and imaging protocols outlined above. For additional MR microscopy using a 9.4 T small-bore MR scanner (Biospec 94/20 USR, Bruker Biospin, Ettlingen, Germany) the eye was moved to a PBS filled stand-alone spherical holder to fit into the magnet bore. Two sets of GRE and RARE imaging were conducted using a 35 mm quadrature volume resonator for TX/RX:

- MR microscopy protocol: FOV=35 mm, matrix size=512x512, in-plane spatial resolution=68 µm, BW=300 Hz/Px; GRE: TR=30 ms, TE=4.4 ms, nominal flip angle =10°, slice thickness=350 µm, RARE: TR=11931 ms, TE=47 ms,

nominal refocusing flip angle=180°, slice thickness=333 µm, inter-echo spacing=11.8 ms, echo train length=12.

- Low resolution protocol: FOV=70 mm, matrix size=256x256, in-plane spatial resolution=0.3 mm, slice thickness=1.0 mm, 32 slices, BW=300 Hz/Px; GRE: TR=30 ms, TE=4.4 ms, nominal flip angle=10°; RARE: TR=3931 ms, TE=52 ms, nominal refocusing flip angle=180°, inter-echo spacing=8.7 ms, echo train length=12.

Imaging artifacts in ex vivo human eyes with ocular tumor

After enucleation of a bulbus equipped with OTMs obtained from a patient with a therapeutically non-responsive intraocular tumor, an assessment of susceptibility artifacts was performed at 7.0 T and additionally at 9.4 T. At 7.0 T the globe was placed in the head phantom described above. The holders were filled with an isotonic 0.9% NaCl solution (B. Braun Melsungen AG, Melsungen, Germany). MR hardware/protocols were identical to the phantom study. In addition, diffusion weighted MRI using a RARE variant (22) was performed: FOV=70 mm, matrix size=192x192, in-plane spatial resolution=0.4 mm, slice thickness=3.0 mm, 1 slice, BW=350 Hz/Px, TR=3300 ms, TE=78 ms, nominal refocusing flip angle=180°, b-values=0, 100, 200, 300, 400 s/mm².

For complementary MR microscopy at 9.4 T the globe was placed in a spherical holder filled with NaCl solution. Three series of imaging were performed:

- GRE: FOV=30 mm, matrix size=512x512, in-plane resolution=59 µm, slice thickness=300 µm, TR=230 ms, TE=10 ms, nominal flip angle=29°, BW=116 Hz/Px.
- RARE: FOV=30 mm, matrix size=256x256, in-plane resolution=117 µm, slice thickness=600 µm, TR=2300 ms, TE=27.5 ms, inter-echo spacing=11.8 ms, nominal refocusing flip angle=90°, BW=195 Hz/Px.
- DWI-RARE: b=0, 200, 500 s/mm², FOV=30 mm, matrix size=256x256, in-plane resolution=117 µm, slice thickness=600 µm, TR=2300 ms, TE=27.5 ms, inter echo spacing=11.8 ms, nominal refocusing flip angle=90°, BW=195 Hz/Px.

Results

Magnetically induced displacement

Magnetic deflection angle measurement showed no measurable deflection from the vertical axis, staying well below the 45° reference point (28). With this finding any risk imposed by magnetically-induced deflection force to an OTM is much smaller than any risk evoked by the gravitational field.

RF power deposition: Real implant vs. disk approximation

EMF simulations of an OTM yielded a non-uniform surface current distribution with a high current density located in the narrow passages bordering the holes as shown for the example of ϑ_2=45° (Fig.1e), which presented the highest maximum surface currents. Approximating the implant with a disk induces lower surface currents with differences of up to -25% (Fig.1f). If the maximum SAR observed for the OTM is benchmarked against the maximum SAR obtained for a disk with the same geometry except for the holes, we found no discrepancy for any investigated orientation ϑ_i for SAR_{1g} as well as for $SAR_{0.01g}$ (Fig.1g). With this finding, we conclude that the disk provides a reasonable approximation of an OTM. This approximation has thus been applied for all further simulations.

SAR averaging mass considerations

EMF and temperature simulations were performed for our SAR averaging mass considerations. Fig.2 illustrates point SAR (per mesh cell) and SAR_{1g} with and without the implant analog being present in the phantom. Averaging over 1g masses levels out the SAR increase caused by the implant analog, as it can be appreciated when comparing $SAR_{1g,disk}$ (Fig.2a) with point SAR_{disk} (Fig.2b). The induced SAR increase after averaging over m_{ave}=1 g is not only spatially indistinguishable but also smeared to the level of the baseline SAR in the TSM (Fig.2c,d). With this finding, an accurate evaluation of the local SAR caused by an OTM requires m_{ave}<1 g.

The SAR averaging mass should predict an RF power distribution reflecting the spatial extent of the potential additional heating caused by the implant (Fig.2e). To permit this comparison in RF power/heat distribution, one specific time point of the heating paradigm has to be selected. For long RF heating periods of small implants, the implant induced temperature increase is surpassed by the baseline heating generated by the RF antenna (31). This transition manifests itself in a temporal heating curve exhibiting a linear temperature increase showing the same slope $\Delta T/dt$ with and without the device under investigation (Fig.2f). In our case of continuous heating (P_{in}=1 W), the transition time was found to be 4 s after the onset of the heating paradigm. The thermal distribution was thus evaluated after a period of 4 s of continuous heating (Fig.2e).

The spatial extent of SAR and temperature hot spots can be considered as a point spread function (PSF; Fig.3a,b). In our case, each hot spot (i.e. each peak on

a profile drawn through the SAR hot spot) presents a PSF that needs to be sufficiently resolved after applying the mass averaging that acts as a broadening filter. Averaging over a mass of 1 g widens the PSF to the extent where the peaks at the tip of the implant analog are no longer recognizable (Fig.3c). At the same time, the overlap of the broadened peaks introduces increased SAR_{1g} near the center of the implant. This contradicts the point SAR distribution, where the bending of the electric field lines causes a shielding effect of this region with point SAR dropping almost to 0 W/kg (Fig.3a), resulting in a low temperature increase (Fig.3b).

A qualitative and quantitative examination of point SAR (Fig.3a), temperature (Fig.3b) and SAR_{ave} (Fig.3c) distributions was carried out along profiles running parallel to the long axis of the RF antenna and through the center of the short axis of the phantom (Fig.3a). To assess SAR and temperature increase due to the implant analog, the baseline obtained for TSM was subtracted as an offset. The resulting profiles represent the increase in SAR (ΔSAR) and temperature (ΔT) induced by the implant analog. ΔSAR profiles were evaluated at two different distances to the antenna. Profile I goes through the center of a slice placed at a depth of d=23.95 mm (Fig.3a), being slightly above the implant in order to investigate the overlapping of the two PSFs. Profile II (d=24.95 mm) covers the location of the SAR_{max} and the implant analog. To quantify the spatial extent of the hotspot obtained from the temperature as well as SAR simulations, the full width at half maximum (FWHM) was calculated for the left peak of profile II in the distribution of point SAR (ΔSAR, Fig.3a), temperature (ΔT, Fig.3b) and SAR_{ave} (ΔSAR, Fig.3c and Fig.4).

As a starting point for applying different SAR averaging masses, we approached the problem considering the sampling theorem. The distance between the two hot spots (i.e. the diameter of the OTM) is 2.5 mm. In order to depict the details accurately, the Nyquist theorem requires sampling with a resolution of 1.25 mm (37). With the TSM density of ρ=1.04 g/cm³, this results in an averaging mass of only m_{ave}=0.002 g. Not only is this mass a factor of 500 smaller than the smallest commonly used averaging mass of SAR_{1g}, it can be also debated as to what extent the computational downscaling of investigated spatial distributions is still applicable to the complex (thermoregulatory) system of the human body. Addressing this limitation, we sought to find the largest averaging volume that would accurately depict the PSF of the ΔT profile. The acceptable discrepancy between FWHM(ΔT) and FWHM(ΔSAR) was set at 15%. An additional consideration of profile I showed the expected increase of SAR_{ave} above the center of the implant analog for all averaging masses. For averaging masses m_{ave}>0.015 g, a third hotspot appeared above the center of the implant analog (Fig.4a,b). This is caused by the overlap of the two PSFs, which underlines the need for a smaller averaging volume. In combination with the evaluation of profile II, this returned a SAR averaging mass of m_{ave}=0.01 g (Fig.4d), resulting in a cube length of a_2=2.1 mm in the TSM. $SAR_{0.01g}$ was thus used for further evaluation.

SAR transfer function

Next, we studied SAR as a function of the position and orientation of the implant analog with respect to the electric field lines. EMF simulations of the disk revealed $SAR_{0.01g}$ peak values that follow an exponential decay with increasing distance between the antenna and the implant ($R^2=1$; Fig.5a). Observing the same behavior in a uniform TSM phantom ("baseline SAR", Fig.5b), a linear correlation was found between $SAR_{0.01g(w)}$ induced by the disk and $SAR_{0.01g(w/o)}$ without the disk, with $SAR_{0.01g(w)}=1.54 \cdot SAR_{0.01g(w/o)}$, $R^2=1$ (Fig.5c). While SAR_{1g} showed the same behavior as $SAR_{0.01g}$, fitting the data of the disk against baseline SAR_{1g} revealed a correlation of only $SAR_{1g(w)}=1.005 \cdot SAR_{1g(w/o)}$ ($R^2=1$), quantitatively confirming the smearing due to the large averaging volume.

When the implant analog was rotated around an axis perpendicular to the E-field lines, thus changing the effective conductive length, a cosine dependence of peak $SAR_{0.01g}$ on the rotation angle $\gamma_{\perp}$ was found (Fig.5d). For further analysis, the data was normalized to the maximum and fitted to a cosine function ($R^2=0.96$; Fig.5e). Again, this effect was not visible in the SAR_{1g} data, yielding constant values for all orientations. Rotation along the E-field lines $\gamma_{\parallel}$ did not alter the effective conductive length and did not show an angular dependence of peak $SAR_{0.01g}$ (Fig.5f) or SAR_{1g}.

By fitting local peak $SAR_{0.01g}$, a transfer function was derived. This transfer function enables an *a priori* estimation of induced $SAR_{0.01g(w)}$ in the presence of the implant based on its rotation perpendicular to the electric field lines and baseline $SAR_{0.01g(w/o)}$ caused by the RF antenna without the presence of the implant (Fig.5g).

$$SAR_{0.01g(w)}(\gamma)=1.54 \cdot (0.1 \cdot \cos(2\gamma_{\perp})+0.87) \cdot SAR_{0.01g(w/o)}+0.3 \text{ W/kg} \quad (1)$$

The constant offset of 0.3 W/kg was added as a safety margin to compensate for underestimation of the simulated data introduced by the fitting process.

Maximum $SAR_{0.01g}$ of 2.64 W/kg in the presence of the implant analog was found for d=15 mm and $\gamma_{\perp}=0°$. $SAR_{0.01g}$ at the surface of the phantom centered underneath the antenna was $SAR_{0.01g(surface)}=2.68$ W/kg. For $m_{ave}=1$ g, a maximum power deposition was found at the phantom surface $SAR_{1g(surface)}=2.26$ W/kg while maximum $SAR_{1g(disk)}=1.74$ W/kg was exhibited at a distance of d=15 mm.

RF induced heating

In all cases, the maximum SAR was found at the phantom surface. Only locations with sufficient distance to the surface were included in the evaluation, ensuring SAR averaging in the homogeneous TSM only. For $m_{ave}=0.01$g (averaging cube length $a_{0.01g}=2.11$ mm) highest $SAR_{0.01g}$ was found at d=1.15mm within the TSM, centered underneath the RF antenna. This is consistent with the averaging volume constituted of homogeneous TSM at the shortest distance to the power source. The larger averaging volume of $m_{ave}=1$g with $a_{1g}=9.8$ mm exhibited highest SAR_{1g} at d=4.65mm. The temperature increase denoted as $\Delta T_{surface}$ was extracted at the position of the maximum SAR_{ave} used for P_{in} normalization. The temperature

increase at the implant analog ΔT_{disk} was evaluated at the position of maximum $SAR_{0.01g}$. The same location was used for the reference ΔT_{TSM}.

Thermal simulations provided a super-linear implant related temperature increase right after the onset of RF power (Fig.6a). After 4 s of heating a linear temperature increase was found. The slope $\Delta T_{disk}/dt$ was identical with the $\Delta T_{TSM}/dt$ obtained for the same phantom location and setup but without the implant analog. This indicates that the thermal flux along the temperature gradient of the hot spot at the implant reached equilibrium with the surrounding tissue. It also suggests that a purely SAR-based estimation of temperature increase is likely to overestimate induced heating near an implant (blue line in Fig.6a). After only 2 s of heating, the temperature at the implant analog was surpassed by the temperature at the phantom surface ($\Delta T_{surface}(2s)$=1.3 mK, $\Delta T_{disk}(2s)$=1.2 mK). This indicates a transition from an implant-dominated heating regime (t<2 s) to a surface-dominated heating regime (t>2 s). The relation was maintained until the end of the heating paradigm. The simulation (P_{in}=1 W, duration t_{RF}=6 min) yielded a total temperature increase of $\Delta T_{surface}$=185 mK at the phantom surface and ΔT_{disk}=103.1 mK at the disk. When compared with the heating curves obtained for the TSM without the implant analog, the presence of the disk in the phantom caused an additional maximum heating of $\delta T_{disk\text{-}TSM}$=1.4 mK. The same behavior

When scaling P_{in} to the normal operating mode (NM) and 1st level controlled mode (CM), peak $SAR_{0.01g}$=10 W/kg caused a temperature increase of ΔT_{max}=641.3 mK at the surface and ΔT_{disk}=381.7 mK at a baseline SAR of $SAR_{0.01g(W/O)}$=3.66W/kg (Fig.6b, Table 1). Additional heating with respect to the TSM was δT_{max}=5.2 mK. The CM (SAR_{ave}=20 W/kg) resulted in ΔT_{max}=1283.1 mK at the surface and ΔT_{disk}=763.4mK. Additional heating with respect to the TSM was δT_{max}=10.4 mK. Scaling P_{in} to obtain ΔT_{max}=1 K limited the input power such that max $SAR_{1g,max}$=12.3 W/kg and $SAR_{0.01g,max}$=15.5 W/kg. In all cases, the highest temperature increase occurred at the phantom surface.

When extending the simulation time to 15 min to cover typical clinical scan times (38-40), surface temperature exceeded ΔT_{max}=1 K for the normal as well as the 1st level controlled mode. This temperature increase was reached with max($SAR_{0.01g(W/O)}$)=3.02 W/kg and max($SAR_{1g(W/O)}$)=2.81 W/kg. In all cases, maximum temperature increase was found at the phantom surface.

With increasing input power, the temperature difference between the disk and TSM as well as the temperature margin between disk and surface increases (Table 1). However, the transition time from a SAR_{disk}-dominated to $SAR_{baseline}$-dominated regime was found to be t_{trans}=4 s in all cases. Increasing the heating time from 6 min to 15 min showed a constant offset $\delta T_{surface\text{-}disk}$ ($\pm 2 \cdot 10^{-4}$ K) for all levels of input power. This supports the theory of an underlying equilibrium with the magnitude of the offset depending on the input power.

Imaging artifacts in phantoms

Fig.7 summarizes the susceptibility artifacts acquired for the uniform agarose phantom using the GRE and RARE protocols. Size and shape differ with changing orientation of the OTM and the imaging plane with respect to B_0. Alignment of the long axis of the implant with B_0 increases the susceptibility artifact in this direction. Maximum artifact size was (8.4x7.5) mm² for the GRE and (8.0x7.8) mm² for the RARE protocol.

Imaging artifacts in ex vivo porcine eyes

Fig.8 surveys susceptibility artifacts obtained from ex vivo pigs' eyes at 7.0 T and 9.4 T. The GRE protocol showed significant susceptibility artifacts induced by the OTM. The RARE protocol was less prone to susceptibility artifacts related to the OTM. At 7.0 T, maximum artifact size was (4.6x7.2) mm² for the GRE and (3.2x4.2) mm² for the RARE protocol for which the extension of the susceptibility artifact towards the vitreous humour barely exceeds the thickness of the sclera.

No major differences in artifact geometry and size were found at 7.0 T and 9.4 T. Maximum artifact size acquired with low resolution at 9.4 T was (4.1x6.9) mm² for the GRE and (3.3x 4.8) mm² for the RARE protocol. The high resolution GRE protocol helped to reduce the artifact size to (2.6x6.3) mm² due to a smaller voxel size and a higher bandwidth per anatomy.

Imaging artifacts in ex vivo human eyes with ocular tumor

Fig.9 surveys the 7.0 T (Fig.9a-c) and 9.4 T (Fig.9d-f) MRI results for an enucleated human eye. GRE and RARE imaging clearly display the ocular mass, severe retinal detachment and the retained fraction of the vitreous humour. The 7.0 T data include a susceptibility artifact caused by the OTM marked by an arrow (Fig.9a-c). Maximum artifact size was (6.0x7.4) mm² for the GRE and (5.5x6.5) mm² for the RARE protocol.

ADC maps obtained at 7.0 T and 9.4 T show a clear delineation of subretinal space, the tumor and the vitreous humour. ADC's obtained at 7.0 T accord with those derived from DWI at 9.4 T: $ADC_{subretinal\ space,7T}=(1.75\pm0.11)\cdot10^{-3}$ mm²/s vs. $ADC_{subretinal\ space,9.4T}=(1.84\pm0.05)\cdot10^{-3}$ mm²/s, $ADC_{tumor,7T}=(0.58\pm0.29)\cdot10^{-3}$ mm²/s vs. $ADC_{tumor,9.4T}=(0.57\pm0.13)\cdot10^{-3}$ mm²/s, $ADC_{vitreous\ humour,7T}=(0.22\pm0.06)\cdot10^{-3}$ mm²/s vs. $ADC_{vitreous\ humour,9.4T}=(0.22\pm0.05)\cdot10^{-3}$ mm²/s).

Discussion

This is the first study that examined the potential MR safety hazards and MR compatibility issues of ocular tantalum markers for ophthalmic MRI at 7.0 T.

From the methodological point of view, our numerical simulations show that an OTM can be conveniently approximated by a disk. Our SAR averaging mass considerations demonstrated a strong need to use averaging masses that are three orders of magnitude smaller than m_{ave}=10g provided by IEC guidelines to accommodate the small size of an OTM for an accurate SAR assessment.

The EMF simulations helped to derive a transfer function which describes local $SAR_{0.01g}$ induced by an OTM interfering with *E*-fields generated by an arbitrary RF coil configuration. This generalization allows SAR assessment without the need for EMF simulations with the OTM being integrated. The proposed transfer function can be incorporated into state-of-the art SAR prediction concepts (41, 42) to provide SAR estimations induced by OTMs for arbitrary RF pulses used for transmission field shimming (43, 44) or parallel transmission (45, 46).

The performed deflection angle measurements demonstrated that any risk imposed by magnetically-induced deflection force to an OTM is much smaller than any risk evoked by the gravitational field. Considering that an OTM is sutured to the sclera in an in vivo situation, it is highly unlikely that interference with the magnetic field will induce any displacement of an OTM. This finding correlates well with prior assessment of the negligible ferromagnetism of tantalum implants (47, 48). This conclusion applies to 7.0 Tesla MR as well as to 1.5 T and 3.0 T MR, since the strongest magnetic B_0 gradient is similar for these instruments. This finding adds to the literature since to the best of our knowledge, no data on the MR safety of OTMs has been presented for the current clinically relevant static magnetic field strengths.

RF heating induced by an OTM is another safety concern addressed in this work. At 7.0 T the RF wavelength λ in orbital muscle, brain tissue and vitreous humour interfacing the sclera is approximately 12-13 cm. This wavelength range exceeds an OTM diameter of 2.5 mm used in clinical practice, so that it is highly unlikely that resonance effects occur at $\lambda/4$ - $\lambda/2$ for OTMs (49). This conclusion applies equally to clinical MR scanners, where the wavelength in orbital muscle, brain tissue and vitreous humour at the interface to sclera is approximately 26-30 cm (3.0 T) or 43-57 cm (1.5 T).

EMF simulations provided a maximum $SAR_{0.01g}$ of 2.64 W/kg (P_{in}=1W) in the presence of an OTM analog. In comparison, a maximum $SAR_{0.01g}$=2.68 W/kg was found for phantom regions closest to the RF antenna, indicating that the OTM did not generate the highest SAR for the target region. An input power of $P_{in,NM}$=3.73 W or $P_{in,CM}$=7.46 W would be feasible while staying within the safety limits established by IEC guidelines. For averaging masses of m_{ave}=1 g, SAR_{1g} a power of $P_{in,NM}$=4.43 W or $P_{in,CM}$=8.85 W can be used without exceeding the limits in the IEC guidelines (26).

The thermal simulations provided valuable insights into how local SAR at the OTM translates into tissue temperature increase and suggested a transition from an implant dominated heating regime (t<2 s) to a surface heating dominated mode (t>2 s). After 4 s of heating a linear temperature increase was found. The slope $\Delta T/dt$ observed in the presence of the OTM analog was identical with $\Delta T/dt$ obtained for the same location and configuration except the OTM, meaning that the properties of the OTM and surrounding tissue act as a heat sink removing temperature from the OTM. Increased input powers scaled to the maximum SAR_{ave} values for the normal operating mode and the 1st level controlled mode as well as maximum temperature rise of 1 K reveal equal transition times of 4 s. When extending the simulation time to 15 min, the offset caused by the implant is constant for all power levels. Taken together, this supports our hypothesis that the temporal occurrence of the equilibrium is linked to the distance between the two hotspots. At the same time, the temperature margin at the end of the heating paradigm between surface, disk analog and TSM increases with increasing input power. Following guidelines limiting the maximum acceptable temperature increase to ΔT_{max}=1 K, the input power was limited such that $SAR_{1g,max}$=3.11 W/kg for the more restrictive SAR_{ave} and the longer heating period of t_{RF}=15 min. Obviously, the increase in temperature obtained for the phantom situation is likely to overestimate the actual temperature rise in vivo. The thermal properties and the thermoregulation (i.e. perfusion) of the tissue that is affected will reduce the temperature increase near the OTM.

It is a recognized limitation of this study that no temperature measurements are included. It has been shown that even for larger implants (i.e. larger hotspots), that changes in temperature sensor positioning of less than 0.5 mm result in erroneous temperature measurements induced by infidelities in the probe placement (50). Considering this finding together with the subtle spatial extent of the temperature hotspot caused by the OTM, no temperature measurements were executed. For similar reasons, this study does not include random positions for temperature assessment as suggested for heating experiments (REF). Due to the overall small increase in temperature caused by the implant when compared to baseline heating, we limited our investigation to the implant position that hinted at the strongest discernable temperature increase.

Finally, the presented work investigated image artifact formation induced by OTMs in order to make a statement on MR compatibility at 7.0 T. If an OTM induces a major susceptibility artifact, this might lead to diagnostic misinterpretations and/or it may mistakenly be attributed to pathology, if it not recognized as an artifact. It is known that subtle metallic implants used in ophthalmology, such as platinum-carrying intraocular lenses and platinum-containing eyelid implants can cause low-level susceptibility artifacts (51, 52). Our T_1-weighted and T_2-weighted phantom imaging studies revealed susceptibility artifacts with a size smaller than 8.5 mm. The artifact size obtained for ex vivo imaging of porcine eyes as well as ex vivo imaging of human eye was smaller (<7.5 mm). T_2-weighted RARE imaging in

ex vivo porcine eyes demonstrated that the extension of the susceptibility artifact towards the vitreous humour barely exceeded the sclera.

The findings of small susceptibility artifacts is in good agreement with prior work, identifying tantalum as a low susceptibility material ($\chi=0.97\cdot10^{-6}$ (53)), causing only small imaging artifacts (54, 55). GRE and RARE imaging of ex vivo human eyes with ocular tumors showed a clear delineation of subretinal space and vitreous humour. RARE-based ADC mapping of ex vivo humans eyes at 7.0 T exhibited a clear discrimination of the tumor mass. These are potential criteria that support an admission of patients with OTMs for MRI at 7.0 T.

One possible indication for 7.0 T imaging is the question whether the tumor has already infiltrated the optic nerve (56). Despite the slightly bigger artifacts of the OTM (5.3 mm for 7.0 T MRI vs. 4.7 mm for 3.0 T MRI) 7.0 T MRI will be of benefit for the treatment planning of ophthalmologic proton therapy: The contours of big tumors should be more realistic. The enhanced spatial resolution would afford an improved differentiation between tumor and retinal detachment. Small extra scleral tumor growth along or in the optic nerve can be detected and modelled in the treatment planning procedure. This allows to irradiate patients with small optic nerve infiltration (up to 3 mm length) with protons and to preserve their eye. The blind spots caused by the artifacts of the OTM placed near the tumor may interfere with its delineation in treatment planning. This can be compensated with other information from fundus photography, ultrasound imaging, and measurements obtained during OTM surgery. Artifacts near the optic nerve are not expected because the distance of the OTM placed near the tumor and the optic nerve is usually greater than 7 mm.

The OTMs investigated in this study were obtained by the only manufacturer providing CE certification for the use of the markers in proton beam therapy of ocular tumors. In conclusion, all ocular tantalum markers commercially available today with CE certification for PRT can be considered safe for MR at field strengths of up to and including 7.0 Tesla.

Acknowledgements

The authors would like to thank Antje Els for her support in setting up the imaging protocols, and Stefanie Kox and Min-Chi Ku for assistance in preparing the pigs' eyes for MR examinations.

Tables

6 min							
SAR limits		NM ($SAR_{0.01g}$)	NM (SAR_{1g})	CM ($SAR_{0.01g}$)	CM (SAR_{1g})	ΔT_{max}=1K at max($SAR_{0.01g}$)	ΔT_{max}=1K at max(SAR_{1g})
P_{in} [W]	1	3.7	4.44	7.4	8.89	5.77	5.44
$\Delta T_{surface,0.01g}$ [mK]	173.0	641.3		1283.1		1000.5	
$\Delta T_{surface,1g}$ [mK]	185.0		814.3		1630.4		997.5
ΔT_{disk} [mK]	103.1	381.7	458.0	763.4	917.1	595.2	561.2
$\delta T_{surface-disk}$ [mK]	69.9/81.9	259.6	356.3	519.7	713.3	405.3	436.3
ΔT_{TSM} [mK]	101.7	376.5	451.8	753.0	904.7	587.2	553.6
$\delta T_{disk-TSM}$ [mK]	1.4	5.2	6.2	10.4	12.4	8	7.6
15 min							
SAR limits		NM ($SAR_{0.01g}$)	NM (SAR_{1g})	CM ($SAR_{0.01g}$)	CM (SAR_{1g})	ΔT_{max}=1K at max($SAR_{0.01g}$)	ΔT_{max}=1K at max(SAR_{1g})
P_{in} [W]	1	3.7	4.44	7.4	8.89	3.05	2.84
$\Delta T_{surface,0.01g}$ [mK]	268.3	1233.9		2557.4		1001.4	
$\Delta T_{surface,1g}$ [mK]	301.8		1614		3302.8		1001.7
ΔT_{disk} [mK]	231.2	911.1	1100	1842.8	2218.0	747.4	694.6
$\delta T_{surface-disk}$ [mK]	37.1/70.6	322.8	514	414.6	1084.8	254	307.1
ΔT_{TSM} [mK]	229.8	905.9	1093.7	1832.3	2205.4	743.1	690.5
$\delta T_{disk-TSM}$ [mK]	1.4	5.2	6.3	10.5	12.6	4.3	4.1

Table 1: Temperature increase obtained for 6 min of continuous RF heating with different input power. ΔT marks the temperature increase at the location "disk", i.e. point of highest $SAR_{0.01g}$ near the implant analog, "TSM", i.e. at the same location but without the implant being present and "surface", i.e. point of highest SAR_{ave} averaged in the continuous virtual phantom. δT denotes the temperature difference between two of these locations (disk vs. TSM and surface vs. disk) after the RF heating.

Figures

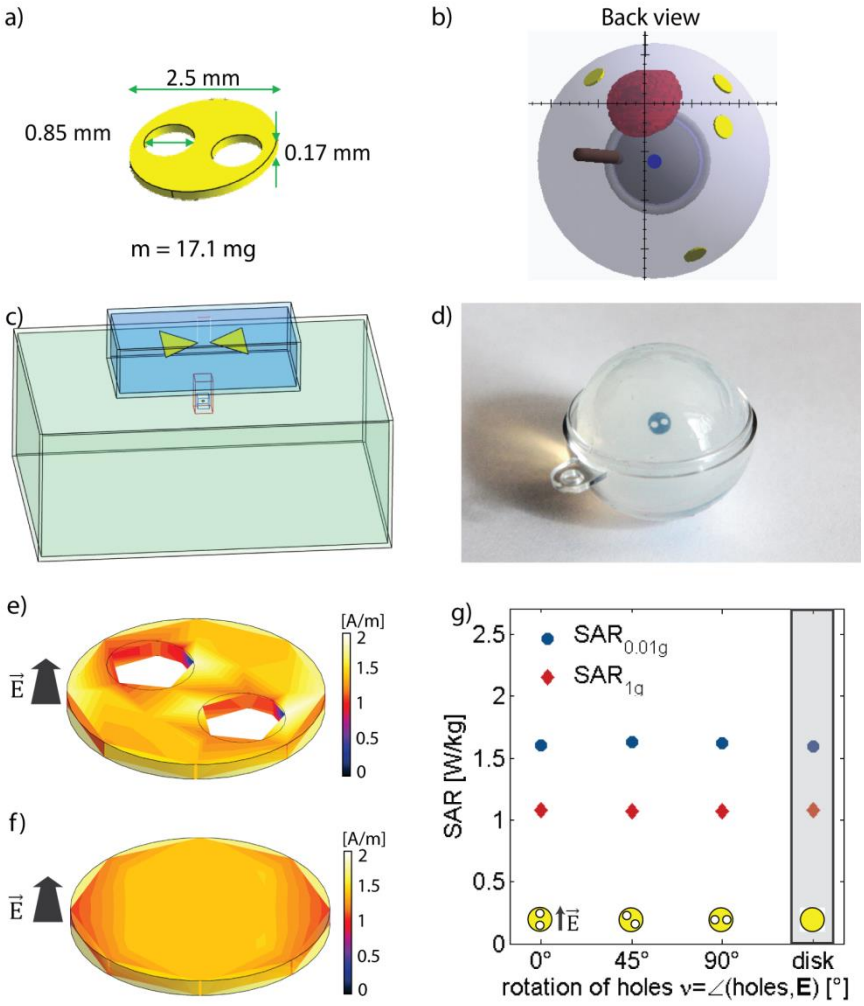

Figure 1: (a) Schematic view of an ocular tantalum marker (OTM) outlining its dimensions. (b) Exemplary location of the tantalum markers (yellow) on an eye (back view) with highlighted intraocular tumor mass (red), optic nerve (brown) and macula (blue). (c) Virtual simulation setup with a bow tie dipole RF antenna building block placed on top of a rectangular PMMA box filled with tissue simulating material (TSM). Two high resolution meshboxes limit the resolution to 0.1 mm isotropic (red) and 0.05 mm isotropic (blue) around the implant. (d=25 mm, $\gamma_{\parallel}=\gamma_{\perp}=0°$). (d) Agarose phantom sample with incorporated OTM placed in the lower half shell of the spherical holder. (e) Absolute value of induced surface current ($P_{in}=1$ W, $\vartheta_2=45°$, d=25 mm, $\gamma_{\parallel}=\gamma_{\perp}=0°$). Maximum surface current of 2.17 A/m is found in the narrowed passage next to the right hole. (f) Absolute value of induced surface current for $P_{in}=1$ W for the disk at the same position. The maximum surface current is 1.64 A/m and up to 25% lower than for the OTM. (g) Induced RF power deposition for implant orientation ϑ_i and for a disk with the same outer dimensions (grey box). For SAR averaging masses of $m_{ave}=1$ g and $m_{ave}=0.01$ g, no difference can be seen for the different surface currents.

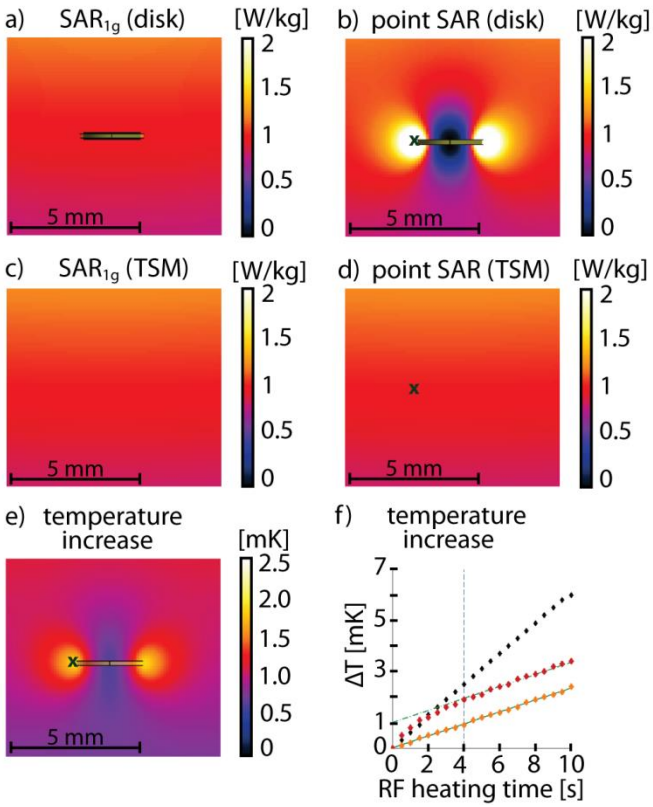

Figure 2: (a,b) Sagittal view of the local SAR distributions obtained for a virtual ocular tantalum marker analog positioned underneath the virtual RF antenna (d=25 mm, $\gamma_{\parallel}=\gamma_{\perp}=0°$). Averaging the induced SAR over masses of 1 g (a) levels out peak values depicted in the meshcell-wise calculation ("point SAR", b) to a point that corresponds to the SAR values found in the homogeneous tissue simulating material (TSM; c,d). (e) Temperature distribution after a heating period of 4 sec. (f) Temperature curves recorded at the point of highest point SAR (green cross in b,d,e) at the rim of the implant analog (red), at the respective position in the homogeneous TSM (yellow) and at in the surface region of the TSM at the point of highest temperature increase (black). The temperature increase caused by the implant analog goes into saturation after 4 s (blue dashed line). Further temperature increase is caused by the baseline RF power deposition, as indicated by the same slope ΔT/dt (green dashed line) when compared to the homogeneous TSM. All simulations: $P_{in}=1$ W.

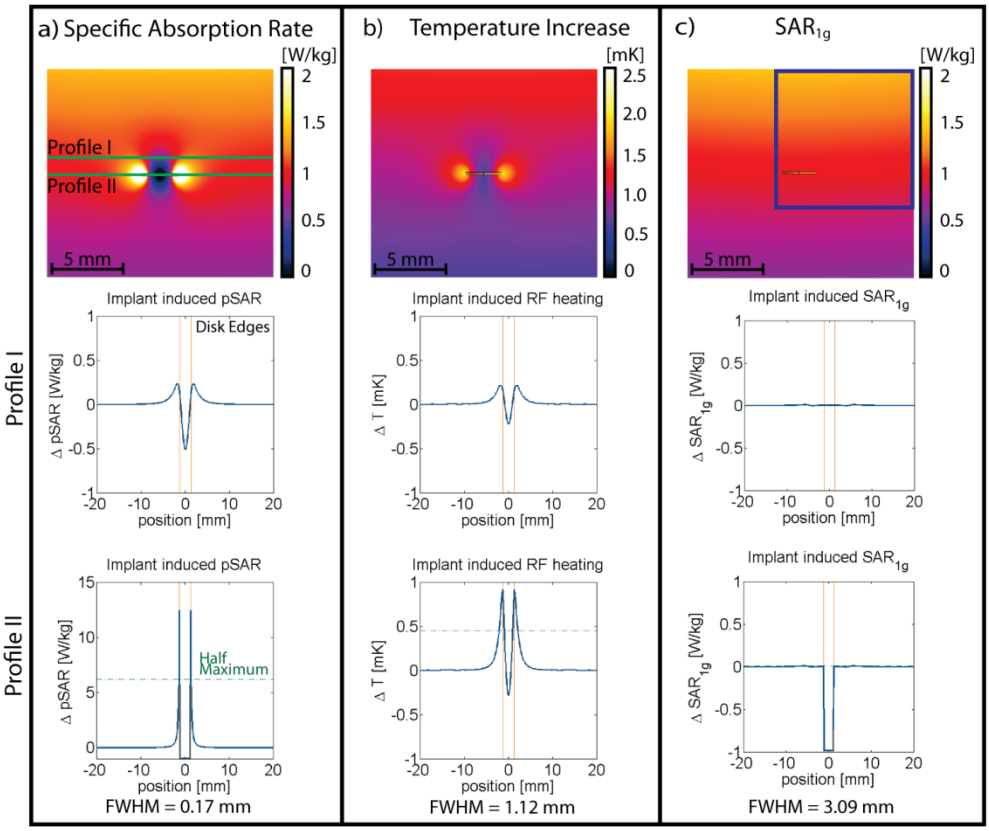

Figure 3: (a) Sagittal view of SAR per mesh cell (0.05 mm isotropic) for a virtual ocular tantalum marker analog (d=25 mm, $\gamma_{\parallel}=\gamma_{\perp}=0°$ $P_{in}=1$ W). Profile I is drawn at a depth of d=23.95 mm, slightly above the implant analog. Profile II represents a line through the SAR maximum near the disk implant at a depth of d=24.95 mm. Both profiles show the increase due to the presence of the implant analog (ΔSAR) after subtraction of the baseline SAR. (b) Temperature distribution and ΔT profiles after a heating period of 4 s. (c) SAR_{1g} distribution. The blue square indicates the face of the averaging cube with a side length of a_{1g}=9.8 mm in the TSM. The ΔSAR profiles represent the SAR increase due to the implant analog.

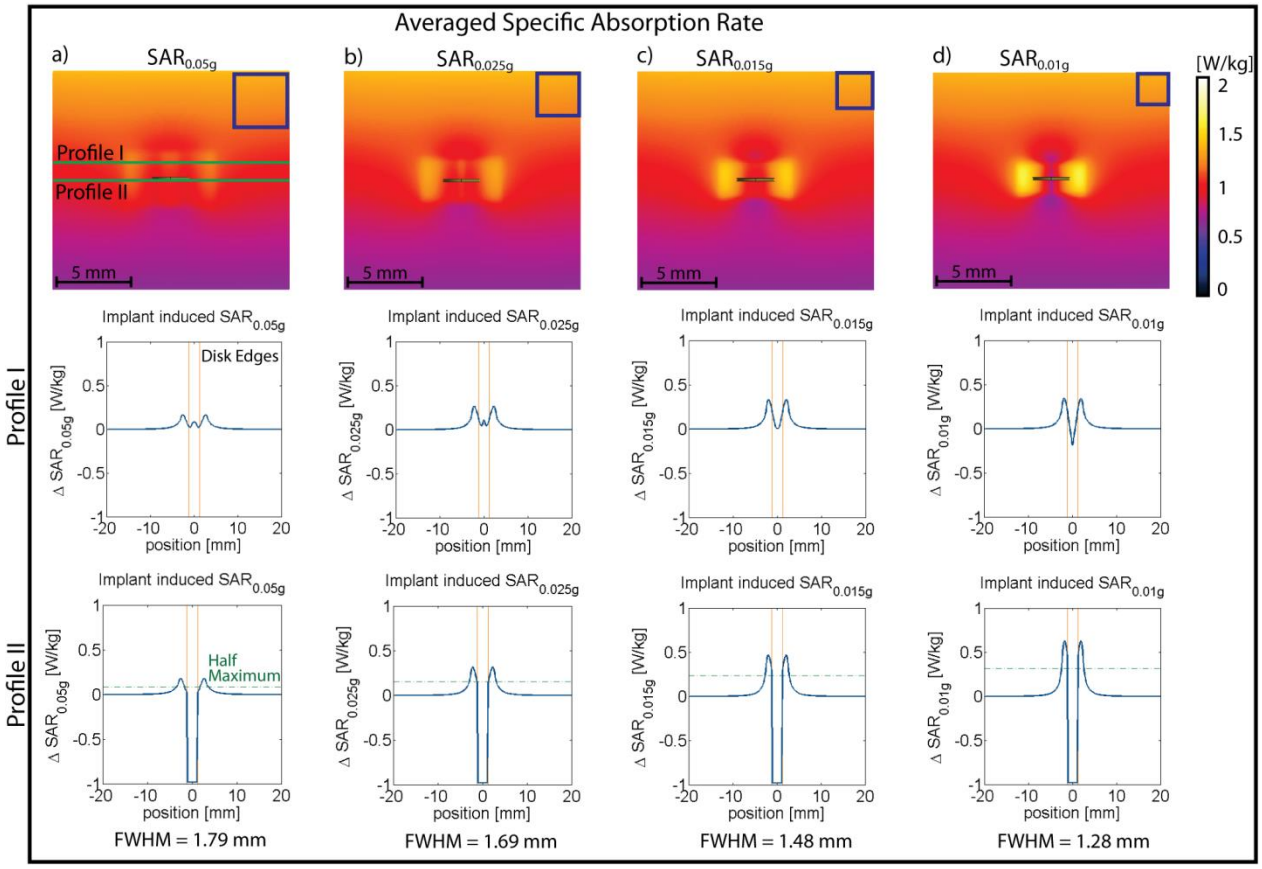

Figure 4: Sagittal view of the SAR distribution for averaging volumes of (a) 0.05 g, (b) 0.025 g, (c) 0.015 g and (d) 0.01 g. The blue squares indicate the faces of the averaging cubes with side lengths of $a_{0.05g}$=3.6 mm, $a_{0.025g}$=2.9 mm, $a_{0.015g}$=2.43 mm and $a_{0.01g}$=2.1 mm in the TSM. $SAR_{0.01g}$ yields no third hot spot in profile I and a broadening of FWHM of less than 15 % in profile II compared to the temperature profile.

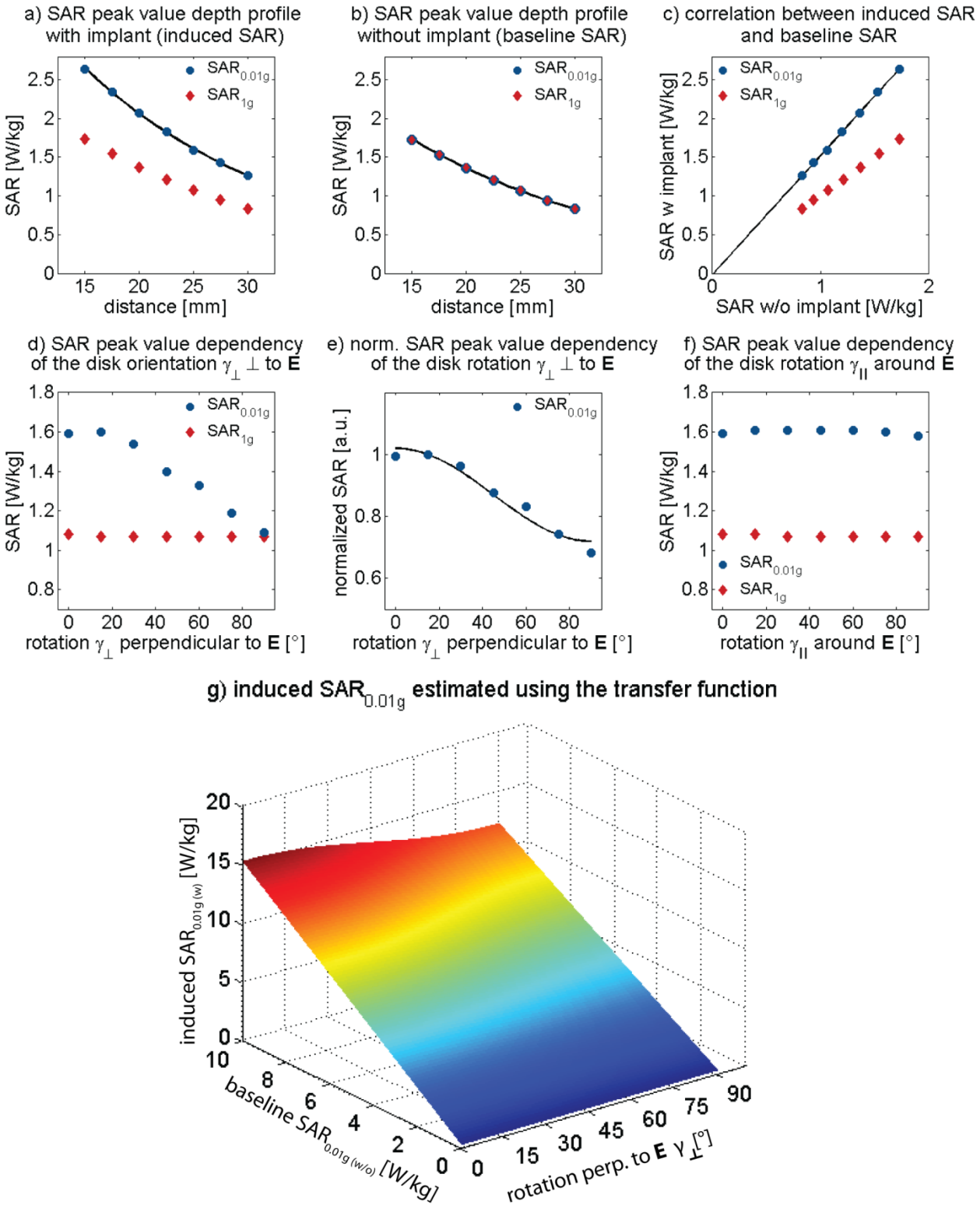

Figure 5: Peak SAR values for $SAR_{0.01g}$ and SAR_{1g}. (a) Induced SAR near the implant analog shows an exponential decay ($R^2=1$) with increasing distance of the disk to the RF antenna. (b) The same behavior can be seen in the uniform TSM ($R^2=1$) suggesting (c) a linear correlation ($R^2=1$) between peak SAR without implant and

peak SAR with implant. While $SAR_{0.01g}$ is increased by a factor of 1.54 vs. baseline, smearing due to the large averaging volume of m_{ave}=1g yields an increase of only 1.005. (d) Rotation $\gamma_{\perp}$ of the disk out of the electric field lines leads to a cosine decay of the $SAR_{0.01g}$ values. (e) The normalized SAR values are fitted to the expected $\cos(2\gamma_{\perp})$ dependence (R^2=0.96). (f) Rotation $\gamma_{\parallel}$ of the disk in the electric field lines shows no angular dependence. (g) $SAR_{0.01g\ (w)}$ induced by the implant analog estimated using the transfer function (equation 1).

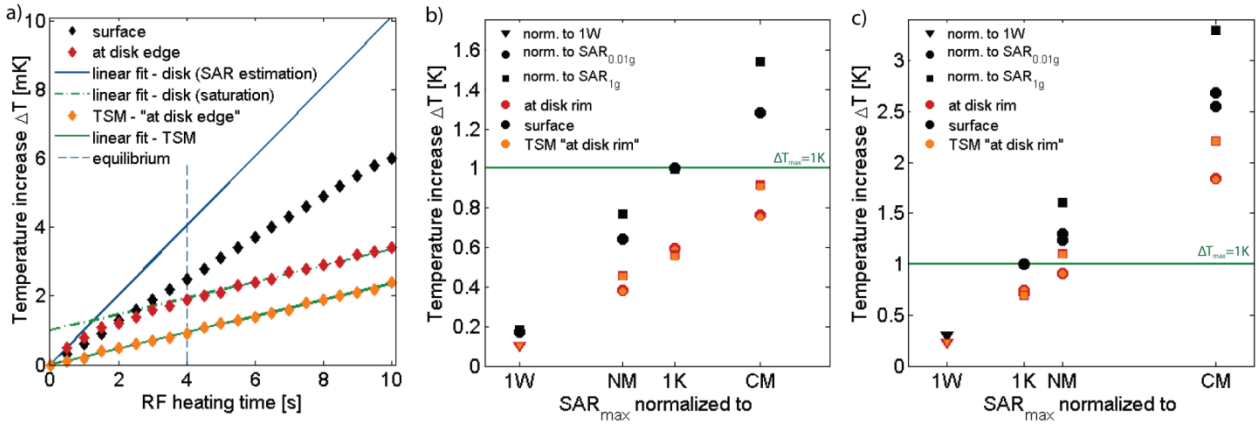

Figure 6: (a) RF heating curves obtained for continuous heating with an input power of P_{in}=1W. The temperature recorded at the point of highest SAR in the vicinity of the implant analog (red) goes into saturation after 4 s (dashed blue line). The subsequent temperature increase follows the same slope ΔT/dt (dashed green line) as observed at the same position in the homogeneous TSM (yellow markers, green line). After only 2 s of RF heating and onwards, the temperature in the vicinity of the implant is surpassed by the temperature increase in the surface region of the phantom (black). Making a SAR based estimation of the temperature increase would not foresee the saturation effect and largely overestimate the resulting temperature increase (blue line). (b,c) Thermal simulation results after 6 min and 15 min of continuous RF heating for P_{in}=1 W, when scaling the input power to the normal mode and the 1st level controlled mode and to a maximum temperature increase of ΔT=1 K. Scaling based on $SAR_{0.01g}$ (dot) and SAR_{1g} (square) yield different input powers and temperatures. All values are listed in table 1.

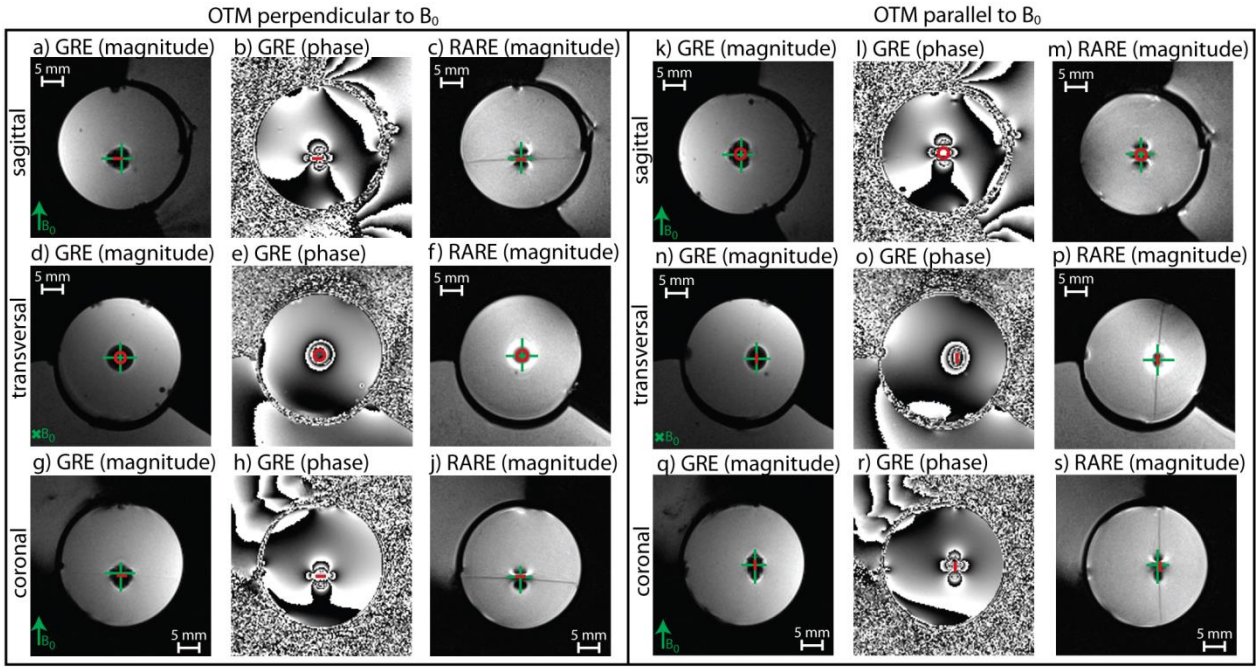

Figure 7: Magnified view of the phantom images acquired at 7.0 T with the implant embedded in a homogeneous agarose sample. The transparent phantom allowed alignment of the implant perpendicular and parallel to the main magnetic field. Rotation of the implant into the magnetic field lines increases the dimension of the susceptibility artifact in the z-direction (sagittal and coronal slices). T_1-weighted gradient echo (GRE) imaging was applied using FOV=70 mm, matrix size=256x256, in-plane spatial resolution=0.3 mm, slice thickness=1 mm, 32 slices, BW=300 Hz/Px, nominal flip angle=4° TR=30 ms, TE=3.9 ms, acquisition time=9:14 min. T_2-weighted rapid acquisition with relaxation enhancement (RARE) imaging was employed with FOV=70 mm, matrix size=256x256, in-plane spatial resolution=0.3 mm, slice thickness=1 mm, 32 slices, BW=300 Hz/Px, TR=3000 ms, TE=55 ms, nominal refocusing flip angle=120°, turbo factor=12, acquisition time=3:20 min. The two protocols show significant differences in artifact shape and prominence but no significant differences in size.

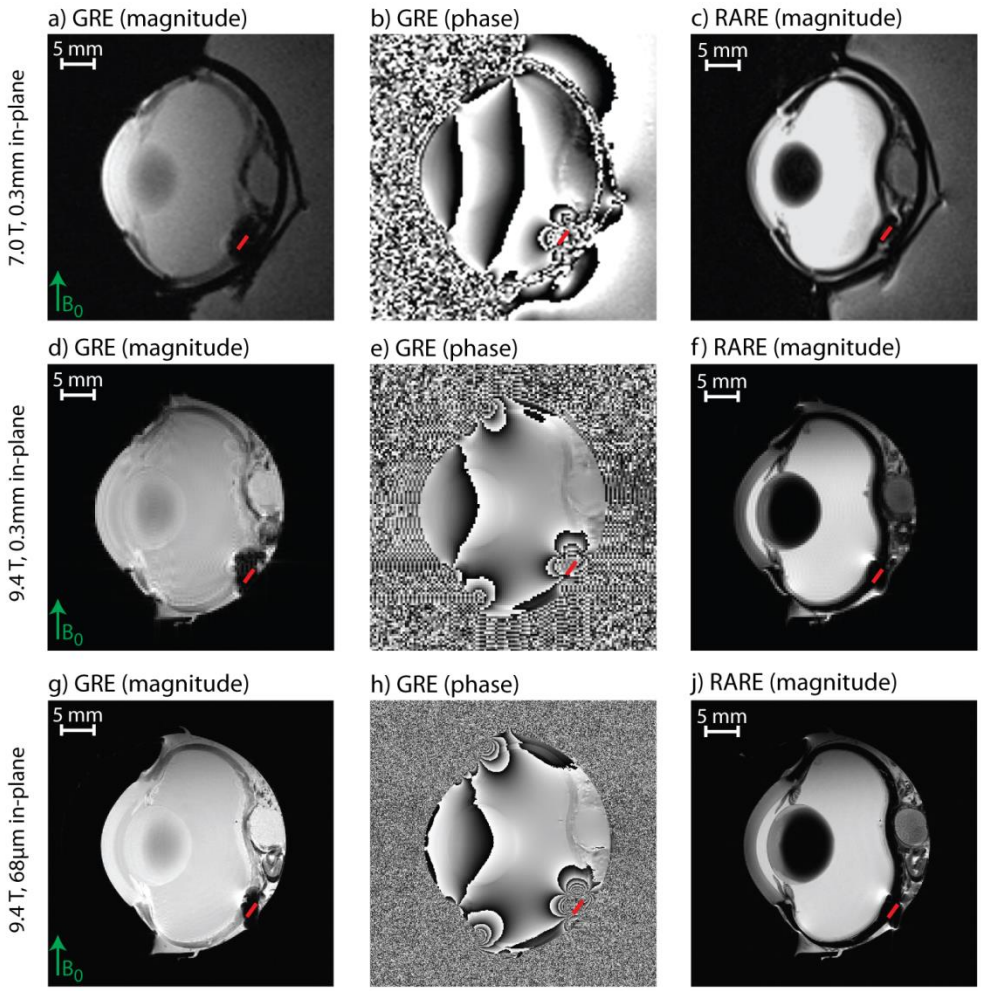

Figure 8: Ex-vivo imaging of a pig eye equipped with three ocular tantalum markers at 7.0 T and 9.4 T. Depicted is the slice with the maximum artifact dimension. The estimated implant position is shown in red. Artifact size obtained for the 7.0 T and 9.4 T GRE protocol is similar to that observed for the homogeneous agarose sample. For RARE imaging the artifact size is approximately half the size of that found for the homogeneous sample.

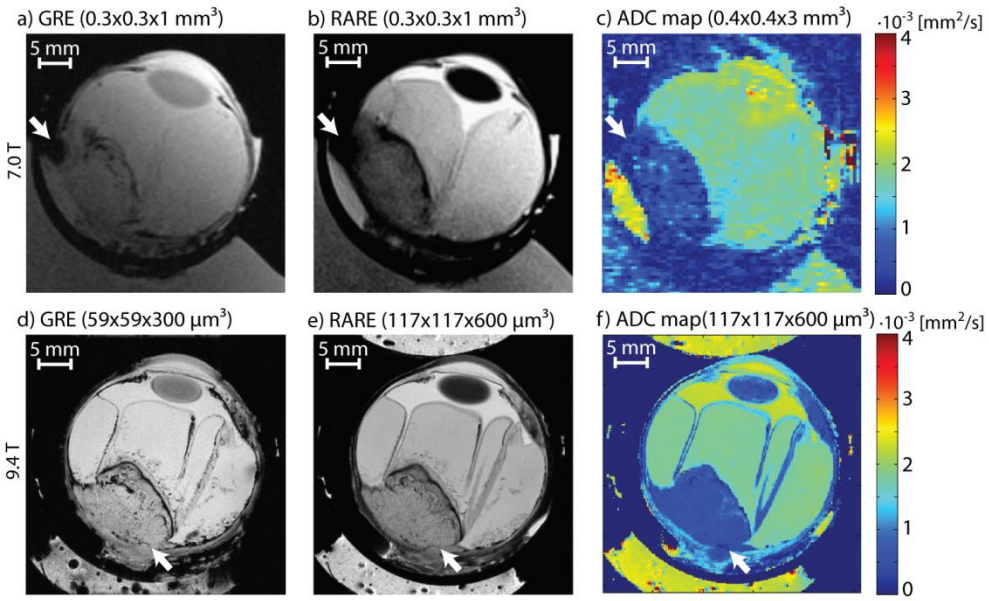

Figure 9: Ex-vivo tumor eye imaging at 7.0 T and 9.4 T. All anatomical images show the delineation of the ocular mass, severe retinal detachment as well as the small remaining fraction of the vitreous humour. The slice selected at 7.0 T (a,b) comprises a susceptibility artifact caused by an ocular tantalum marker (arrow). After transferring the eye ball to a smaller holder for imaging at 9.4 T, the slice position was not reproduced. The slice depicted at 9.4 T (d,e) shows the root of the optic nerve (arrow), separated from the tumor by a slight delineation. Histology confirmed that the tumor had not yet infiltrated the optic nerve. Apparent diffusion coefficients (ADC) obtained at 7.0 T (c) and 9.4 T (f) are in good agreement (7.0 T vs. 9.4 T: subretinal space: $ADC_{7.0T}=(1.75\pm0.11)\cdot10^{-3}$ mm²/s, $ADC_{9.4T}=(1.84\pm0.05)\cdot10^{-3}$ mm²/s; tumor: $ADC_{7.0T}=(0.58\pm0.29)\cdot10^{-3}$ mm²/s, $ADC_{9.4T}=(0.57\pm0.13)\cdot10^{-3}$ mm²/s; vitreous humour: $ADC_{7.0T}=(0.22\pm0.06)\cdot10^{-3}$ mm²/s, $ADC_{9.4T}=(0.22\pm0.05)\cdot10^{-3}$ mm²/s).

References

1. M.F. Mafee, *Uveal melanoma, choroidal hemangioma, and simulating lesions. Role of MR imaging.* Radiol Clin North Am, 1998. **36**(6): p. 1083-1099, x.
2. S. Marnitz, D. Cordini, R. Bendl, A.J. Lemke, J. Heufelder, I. Simiantonakis, H. Kluge, N.E. Bechrakis, M.H. Foerster and W. Hinkelbein, *Proton therapy of uveal melanomas: intercomparison of MRI-based and conventional treatment planning.* Strahlenther Onkol, 2006. **182**(7): p. 395-399.
3. T. Tartaglione, M.M. Pagliara, M. Sciandra, C.G. Caputo, R. Calandrelli, G. Fabrizi, S. Gaudino, M.A. Blasi and C. Colosimo, *Uveal melanoma: evaluation of extrascleral extension using thin-section MR of the eye with surface coils.* Radiol Med, 2014. **119**(10): p. 775-783.
4. C. Ciller, S.I. De Zanet, M.B. Ruegsegger, A. Pica, R. Sznitman, J.P. Thiran, P. Maeder, F.L. Munier, J.H. Kowal and M.B. Cuadra, *Automatic Segmentation of the Eye in 3D Magnetic Resonance Imaging: A Novel Statistical Shape Model for Treatment Planning of Retinoblastoma.* Int J Radiat Oncol Biol Phys, 2015. **92**(4): p. 794-802.
5. Y. Yonekawa and I.K. Kim, *Epidemiology and management of uveal melanoma.* Hematol Oncol Clin North Am, 2012. **26**(6): p. 1169-1184.
6. M. Nielsen, M. Dogrusoz, J.C. Bleeker, W.G. Kroes, C.A. van Asperen, M. Marinkovic, G.P. Luyten and M.J. Jager, *The genetic basis of uveal melanoma.* J Fr Ophtalmol, 2015. **38**(6): p. 516-521.
7. Z. Wang, M. Nabhan, S.E. Schild, S.L. Stafford, I.A. Petersen, R.L. Foote and M.H. Murad, *Charged particle radiation therapy for uveal melanoma: a systematic review and meta-analysis.* Int J Radiat Oncol Biol Phys, 2013. **86**(1): p. 18-26.
8. G.E. Bekkering, A.W. Rutjes, V.V. Vlassov, D.M. Aebersold, K. von Bremen, P. Juni and J. Kleijnen, *The effectiveness and safety of proton radiation therapy for indications of the eye : a systematic review.* Strahlenther Onkol, 2009. **185**(4): p. 211-221.
9. J. Hrbacek, K.K. Mishra, A. Kacperek, R. Dendale, C. Nauraye, M. Auger, J. Herault, I.K. Daftari, A.V. Trofimov and H.A. Shih, *Practice Patterns Analysis of Ocular Proton Therapy Centers: The International OPTIC Survey.* International Journal of Radiation Oncology* Biology* Physics, 2016.
10. E.S. Gragoudas, M. Goitein, A.M. Koehler, L. Verhey, J. Tepper, H.D. Suit, R. Brockhurst and I.J. Constable, *Proton irradiation of small choroidal malignant melanomas.* Am J Ophthalmol, 1977. **83**(5): p. 665-673.
11. C.A. Amstutz, N.E. Bechrakis, M.H. Foerster, J. Heufelder and J.H. Kowal, *Intraoperative localization of tantalum markers for proton beam radiation of choroidal melanoma by an opto-electronic navigation system: a novel technique.* Int J Radiat Oncol Biol Phys, 2012. **82**(4): p. 1361-1366.
12. E.S. Gragoudas, M. Goitein, L. Verhey, J. Munzenreider, H.D. Suit and A. Koehler, *Proton beam irradiation: an alternative to enucleation for intraocular melanomas.* Ophthalmology, 1980. **87**(6): p. 571-581.
13. S. Höcht, N.E. Bechrakis, M. Nausner, K.-M. Kreusel, H. Kluge, J. Heese, J. Heufelder, D. Cordini, H. Homeyer and H. Fuchs, *Proton therapy of Uveal melanomas in Berlin.* Strahlentherapie und Onkologie, 2004. **180**(7): p. 419-424.

14. B. Damato, A. Kacperek, D. Errington and H. Heimann, *Proton beam radiotherapy of uveal melanoma.* Saudi Journal of Ophthalmology, 2013. **27**(3): p. 151-157.
15. I. Daftari, E. Aghaian, J.M. O'Brien, W. Dillon and T.L. Phillips, *3D MRI-based tumor delineation of ocular melanoma and its comparison with conventional techniques.* Med Phys, 2005. **32**(11): p. 3355-3362.
16. C.L. Shields, J.A. Shields, K. Baez, J.R. Cater and P. de Potter, *Optic nerve invasion of retinoblastoma. Metastatic potential and clinical risk factors.* Cancer, 1994. **73**(3): p. 692-698.
17. K. Richdale, P. Wassenaar, K. Teal Bluestein, A. Abduljalil, J.A. Christoforidis, T. Lanz, M.V. Knopp and P. Schmalbrock, *7 Tesla MR imaging of the human eye in vivo.* J Magn Reson Imaging, 2009. **30**(5): p. 924-932.
18. J.B. Christoforidis, P.A. Wassenaar, G.A. Christoforidis, V.Y. Ho, M.V. Knopp and P.M. Schmalbrock, *Retrobulbar vasculature using 7-T magnetic resonance imaging with dedicated eye surface coil.* Graefe's Archive for Clinical and Experimental Ophthalmology, 2013. **251**(1): p. 271-277.
19. J. Beenakker, G. Rijn, G. Luyten and A. Webb, *High-resolution MRI of uveal melanoma using a microcoil phased array at 7 T.* NMR in Biomedicine, 2013. **26**(12): p. 1864-1869.
20. U. Walter, T. Niendorf, A. Graessl, J. Rieger, P.C. Kruger, S. Langner, R.F. Guthoff and O. Stachs, *Ultrahigh field magnetic resonance and colour Doppler real-time fusion imaging of the orbit--a hybrid tool for assessment of choroidal melanoma.* Eur Radiol, 2014. **24**(5): p. 1112-1117.
21. T. Lindner, S. Langner, A. Graessl, et al., *High spatial resolution in vivo magnetic resonance imaging of the human eye, orbit, nervus opticus and optic nerve sheath at 7.0 Tesla.* Exp Eye Res, 2014. **125**: p. 89-94.
22. K. Paul, A. Graessl, J. Rieger, D. Lysiak, T. Huelnhagen, L. Winter, R. Heidemann, T. Lindner, S. Hadlich and A. Zimpfer, *Diffusion-Sensitized Ophthalmic Magnetic Resonance Imaging Free of Geometric Distortion at 3.0 and 7.0 T: A Feasibility Study in Healthy Subjects and Patients With Intraocular Masses.* Investigative radiology, 2015. **50**(5): p. 309-321.
23. T. Lindner, S. Langner, K. Falke, et al., *Anatomic and pathological characterization of choroidal melanoma using multimodal imaging: what is practical, what is needed?* Melanoma Res, 2015.
24. J.M. Beenakker, T.A. Ferreira, K.P. Soemarwoto, S.W. Genders, W.M. Teeuwisse, A.G. Webb and G.P. Luyten, *Clinical evaluation of ultra-high-field MRI for three-dimensional visualisation of tumour size in uveal melanoma patients, with direct relevance to treatment planning.* Magn Reson Mater Phy, 2016. **29**: p. 571-577.
25. F.G. Shellock, *Reference Manual for Magnetic Safety, Implants and Devices,* 2014. 744,
26. IEC, *60601-2-33 Medical electrical equipment - Part 2-33: Particular requirements for the basic safety and essential performance of magnetic resonance equipment for medical diagnosis. Edition 3.0.* 2010.
27. ICNIRP, *ICNIRP Guidelines - For Limiting Exposure to Time-Varying Electric, Magnetic and Electromagnetic Fields (up to 300GHz).* Health physics, 1998. **74**(4): p. 494-522.
28. ASTM International, *Standard Test Method for Measurement of Magnetically Induced Displacement Force on Medical Devices in the Magnetic Resonance Environment*, in *F2052/15*, ASTM International, Editor 2015: West Conshohocken, PA, DOI: 10.1520/F2052-15.

29. P. Hasgall, F. Di Gennaro, C. Baumgartner, E. Neufeld, M. Gosselin, D. Payne, A. Klingenböck and N. Kuster, *IT'IS Database for thermal and electromagnetic parameters of biological tissues*, 2015, DOI: 10.13099/VIP21000-03-0.
30. L. Winter, C. Özerdem, W. Hoffmann, et al., *Design and Evaluation of a Hybrid Radiofrequency Applicator for Magnetic Resonance Imaging and RF Induced Hyperthermia: Electromagnetic Field Simulations up to 14.0 Tesla and Proof-of-Concept at 7.0 Tesla.* PLoS One, 2013. **8**(4): p. e61661.
31. L. Winter, E. Oberacker, C. Özerdem, Y. Ji, F. von Knobelsdorff-Brenkenhoff, G. Weidemann, B. Ittermann, F. Seifert and T. Niendorf, *On the RF heating of coronary stents at 7.0 Tesla MRI.* Magnetic Resonance in Medicine, 2015. **74**(4): p. 999-1010.
32. J.-M. Jin, *Theory and computation of electromagnetic fields,* 2010: John Wiley & Sons. 572,
33. O. Kraff, K.H. Wrede, T. Schoemberg, P. Dammann, Y. Noureddine, S. Orzada, M.E. Ladd and A.K. Bitz, *MR safety assessment of potential RF heating from cranial fixation plates at 7 T.* Medical physics, 2013. **40**(4): p. 042302.
34. J. Wezel, B.J. Kooij and A.G. Webb, *Assessing the MR compatibility of dental retainer wires at 7 Tesla.* Magnetic Resonance in Medicine, 2014. **72**(4): p. 1191-1198.
35. A. Graessl, M. Muhle, M. Schwerter, et al., *Ophthalmic magnetic resonance imaging at 7 T using a 6-channel transceiver radiofrequency coil array in healthy subjects and patients with intraocular masses.* Invest Radiol, 2014. **49**(5): p. 260-270.
36. ASTM International, *Standard Test Method for Evaluation of MR Image Artifacts from Passive Implants*, in *ASTM F2119-07*, ASTM International, Editor 2013: West Conshohocken, PA, DOI: 10.1520/F2119-07R13.
37. C.E. Shannon, *A mathematical theory of communication.* ACM SIGMOBILE Mobile Computing and Communications Review, 2001. **5**(1): p. 3-55.
38. A.R. Rezai, D. Finelli, J.A. Nyenhuis, G. Hrdlicka, J. Tkach, A. Sharan, P. Rugieri, P.H. Stypulkowski and F.G. Shellock, *Neurostimulation systems for deep brain stimulation: In vitro evaluation of magnetic resonance imaging–related heating at 1.5 tesla.* Journal of Magnetic Resonance Imaging, 2002. **15**(3): p. 241-250.
39. M.B. Edwards, K.M. Taylor and F.G. Shellock, *Prosthetic heart valves: evaluation of magnetic field interactions, heating, and artifacts at 1.5 T.* Journal of Magnetic Resonance Imaging, 2000. **12**(2): p. 363-369.
40. O. Majdani, M. Leinung, T. Rau, A. Akbarian, M. Zimmerling, M. Lenarz, T. Lenarz and R. Labadie, *Demagnetization of cochlear implants and temperature changes in 3.0 T MRI environment.* Otolaryngology--Head and Neck Surgery, 2008. **139**(6): p. 833-839.
41. G. Eichfelder and M. Gebhardt, *Local specific absorption rate control for parallel transmission by virtual observation points.* Magn Reson Med, 2011. **66**(5): p. 1468-1476.
42. I. Graesslin, H. Homann, S. Biederer, P. Bornert, K. Nehrke, P. Vernickel, G. Mens, P. Harvey and U. Katscher, *A specific absorption rate prediction concept for parallel transmission MR.* Magn Reson Med, 2012. **68**(5): p. 1664-1674.
43. G.J. Metzger, C. Snyder, C. Akgun, T. Vaughan, K. Ugurbil and P.F. Van de Moortele, *Local B1+ shimming for prostate imaging with transceiver arrays at 7T based on subject-dependent transmit phase measurements.* Magn Reson Med, 2008. **59**(2): p. 396-409.
44. S. Schmitter, L. DelaBarre, X. Wu, A. Greiser, D. Wang, E.J. Auerbach, J.T. Vaughan, K. Ugurbil and P.F. Van de Moortele, *Cardiac imaging at 7 Tesla: Single- and two-spoke radiofrequency*

pulse design with 16-channel parallel excitation. Magn Reson Med, 2013. **70**(5): p. 1210-1219.
45. U. Katscher, P. Bornert, C. Leussler and J.S. van den Brink, *Transmit SENSE.* Magn Reson Med, 2003. **49**(1): p. 144-150.
46. Y. Zhu, *Parallel excitation with an array of transmit coils.* Magn Reson Med, 2004. **51**(4): p. 775-784.
47. F.G. Shellock and J.V. Crues, *High-field-strength MR imaging and metallic biomedical implants: an ex vivo evaluation of deflection forces.* American Journal of Roentgenology, 1988. **151**(2): p. 389-392.
48. F. Shellock and C. Schatz, *Metallic otologic implants: in vitro assessment of ferromagnetism at 1.5 T.* American journal of neuroradiology, 1991. **12**(2): p. 279-281.
49. H. Virtanen, J. Huttunen, A. Toropainen and R. Lappalainen, *Interaction of mobile phones with superficial passive metallic implants.* Phys Med Biol, 2005. **50**(11): p. 2689.
50. E. Neufeld, S. Kühn, G. Szekely and N. Kuster, *Measurement, simulation and uncertainty assessment of implant heating during MRI.* Physics in medicine and biology, 2009. **54**(13): p. 4151.
51. G.A. van Rijn, J.E. Mourik, W.M. Teeuwisse, G.P. Luyten and A.G. Webb, *Magnetic resonance compatibility of intraocular lenses measured at 7 Tesla.* Invest Ophthalmol Vis Sci, 2012. **53**(7): p. 3449-3453.
52. T. Schrom, A. Thelen, P. Asbach and H.-C. Bauknecht, *Effect of 7.0 Tesla MRI on upper eyelid implants.* Ophthalmic Plastic & Reconstructive Surgery, 2006. **22**(6): p. 480-482.
53. F. Hoare and J. Walling, *An absolute measurement of the susceptibility of tantalum and other metals.* Proceedings of the Physical Society. Section B, 1951. **64**(4): p. 337.
54. G. Teitelbaum, H. Ortega, S. Vinitski, H. Stern, J. Tsuruda, D. Mitchell, M. Rifkin and W. Bradley Jr, *Low-artifact intravascular devices: MR imaging evaluation.* Radiology, 1988. **168**(3): p. 713-719.
55. G.P. Teitelbaum, M. Raney, M.J. Carvlin, A.H. Matsumoto and K.H. Barth, *Evaluation of ferromagnetism and magnetic resonance imaging artifacts of the Strecker tantalum vascular stent.* Cardiovascular and interventional radiology, 1989. **12**(3): p. 125-127.
56. A.D. Singh, S.M. Platt, L. Lystad, M. Lowe, S. Oh, S.E. Jones, Y. Alzahrani and T. Plesec, *Optic Nerve Assessment Using 7-Tesla Magnetic Resonance Imaging.* Ocular oncology and pathology, 2016. **2**(3): p. 178-180.